Contributions to Plasma Physics

Contributions to Plasma Physics

ORIGINAL ARTICLE OPEN ACCESS

Heat Load Mitigation Studies in the W7-X Stellarator Experiment

Dirk Naujoks | Amit Kharwandikar | Jasper Dettmar | Michael Endler | Joris Fellinger | Yu Gao | Joachim Geiger | Marcin Jakubowski | Thomas Sieber | Sebastian Thiede | Christian Voß | W7-X Team

Max-Planck-Institut für Plasmaphysik, München, Germany

Correspondence: Dirk Naujoks (dirk.naujoks@ipp.mpg.de)

Received: 29 October 2025 | **Revised:** 18 March 2026 | **Accepted:** 20 March 2026

Keywords: fusion | heat loads | plasma-facing components | Stellarator Wendelstein 7-X

ABSTRACT

During the experiments at the stellarator Wendelstein 7-X (W7-X) with fully water-cooled plasma-facing components (PFC), including carbon-fiber composite (CFC) divertor targets with a thermal load capability of 10 MW/m^2, high performance was achieved. However, weak design points have also been observed by increasing the heating power and discharge time. This primarily impacts the middle part of the divertor units, as well as some baffle and heat shield areas. These areas receive heat loads that exceed their specifications. The extent to which overloading specific components restricts plasma operation for different magnetic field configurations is shown, and the most critical areas are identified. The effects of using different operational actuators to improve the situation are discussed. However, substantial mitigation of excess heat loads under attached plasma conditions is only achievable through design changes to the divertor and baffle areas. Two different geometric modifications to the plasma-facing surface (PFS) are proposed to help extend the operational range of the W7-X with regard to higher heating power, while safeguarding the divertor components.

1 | Introduction

Starting in 2015, the scientific exploration of the W7-X stellarator fusion experiment, operated in Greifswald, Germany, demonstrated high performance in its operational campaigns [1]. Major achievements include proving the accuracy of the magnetic field [2], enabling the required magnetic topology with the delicate island structure at the plasma edge; good control of net toroidal plasma currents ("bootstrap currents"), as predicted [3]; the observation of low collisional (neoclassical) transport [4]; and stable energy detachment operation with the island divertor [5].

Starting with campaign OP2.1 (September 2022–March 2023), the W7-X device is operating with water-cooled first wall components [6], including the divertor and baffle areas. This allows for thermal equilibrium of the wall components during long-pulse operation. The scientific operation campaign OP2.3 of W7-X was successfully conducted in the first part of 2025 (February 2025–May 2025). This campaign followed the operation campaign OP2.2 (October 2024–December 2024) without venting and opening the plasma vessel. With the combined heating power of both the electron cyclotron resonance heating (ECRH) and the neutral beam injection (NBI), record triple products for stellarators of $n_e T_i \tau_E = 1.6 \times 10^{20}\ \mathrm{m^{-3}} \cdot 2.8\ \mathrm{keV} \cdot 0.25\ \mathrm{s} > 10^{20}\ \mathrm{m^{-3}}\ \mathrm{keV\,s}$ could be achieved for 2 s (experiment program XP_20241204.72) [7]. Slightly lower values have been obtained for up to 14 s by using the newly installed steady-state pellet systems [8] to maintain the core plasma density at high levels of about $n_e = 1.4 \times 10^{20}\ \mathrm{m^{-3}}$ (XP_20250327.46) [9].

The full list of W7-X team members is given in O. Grulke et al., *Nuclear Fusion* 64 (2024): 112002.

Turbulence suppression by tailoring the density profiles [7] enabled reaching energy confinement times τ_E of up to 600 ms (XP_20250520.41). Achieving such performance requires high heating power. However, the experiments have shown that increasing the input power leads to overheating of certain components, even at a relatively low input power of about $P_{ECRH} \simeq 4-5$ MW, depending on the different magnetic field configurations and operation settings. Clearly, excess heat loads endanger the planned upgrades to the heating capability of both ECRH and NBI for the upcoming OP2.4/OP2.5 campaigns, which aim to reach a combined input power of 15 MW.

Several factors determine the heat load pattern and peak loads. First, the magnetic field configuration defines the island topology, which then determines the strike-line pattern on the divertor components. Error field correction is applied using trim coils to reduce heat load asymmetry [10]. The control coils can transform the islands at the plasma edge by making them smaller or larger or by shifting them poloidally. They can also be operated in two different sweep modes. All of this results in a modified heat load pattern [11].

Even with low values of several kA in a stellarator such as W7-X, the plasma current modifies the strike-line positions [12] and can move peak heat loads toward thermally weaker components during the discharge itself when the build-up of bootstrap currents takes more than 10 s. Successful attempts have been made to counteract this using electron cyclotron current drive (ECCD). This enabled a long pulse operation of approximately 300 s under attached plasma conditions (XP_20241212.55). It was also tested to compensate for the change in the iota, induced by the toroidal plasma current, by modifying the currents in the planar coil system together with counter-ECCD.

Active impurity seeding reduces convective loads on the targets by increasing radiation losses. This was demonstrated with radiation power of up to 10 MW in the case of feed-forward seeding using neon (program XP_20250506.082 with $P_{ECRH} = 5$ MW, $P_{NBI} = 7.2$ MW). Feedback-controlled seeding using neon allowed reaching levels of up to 6 MW of radiation power P_{rad}, while using nitrogen as the injected impurity gas allowed reaching levels of up to 4.5 MW. With a controlled radiation level of $P_{rad} = 4$ MW using neon injection via the divertor gas inlet system, a high-performance pellet scenario could be extended to 40 s without overloading the components (XP_20250522.49, $P_{ECRH} \simeq 5-6$ MW) [9]. A discharge with $P_{ECRH} = 5$ MW could be prolonged to about 6 min with feedback-controlled seeding at approximately $P_{rad} = 4$ MW (XP_20250520.11). This is the highest total energy input reached so far in W7-X: 1.8 GJ. The plan is to improve and develop the feedback–control functionality further to protect the components from excess loads at higher heating power. However, during the initial attempts in OP2.3 to develop combined core-edge scenarios with high core parameters while maintaining safe heat loads, it was discovered that increased radiation losses from injected impurity gases could deteriorate the favorable density gradients within the confined region, close to the last closed flux surface (LCFS). High-performance discharges in W7-X are characterized by steep plasma density gradients (density peaking), which significantly suppress anomalous turbulent transport. However, this also leads to increased inward convection of impurities, especially those with higher Z. The radiation does not remain in the edge plasma; rather, it begins to creep into the confined regions when the radiation fraction is greater than 0.6. This depends on the magnetic field configuration. This is a delicate balance that requires optimizing the different scenarios with and without ECRH, NBI, or pellets. Relaxing the limitations of the divertor components would increase flexibility by developing such scenarios.

This study demonstrates how modifying the plasma-facing surfaces of specific target and baffle modules can mitigate the limitation of overloaded divertor components. Different magnetic field configurations are assessed (Section 2) with respect to the areas with the highest heat loads (Section 2.2), which result in high surface temperatures as measured by the IR thermography system at W7-X (Section 2.1). The limitations of the divertor components are described in Section 2.2. As described in Section 3, modifying the middle part of the divertor should also protect nearby loaded components. A redistribution of loads is envisaged by exchanging the outer baffle with targets capable of withstanding higher heat loads, such as divertor targets. In addition, the movement of these modules toward the plasma is suggested. This works not only for one selected magnetic field configuration, as shown in Section 4.

2 | Operation Limitations

The extensive magnetic configuration space of W7-X [13, 14] has been exploited in OP2.2/OP2.3, including reversed field operation for certain configurations. For our study, we analyzed the 16 configurations listed in Table 1, which represent a subset of the 23 main configurations run in these two campaigns. The number of discharges that the session leaders rated as "Result: ok," excluding test and conditioning discharges, is given in the last column of the table. As can be seen, the standard configuration dominated the experimental program, followed by the high-mirror and high-iota configurations.

2.1 | Surface Temperature Measurements

Surface temperature measurements were conducted using an infrared (IR) thermography system for all of these discharges. A total of 13 IR cameras have been installed in OP2.2/OP2.3 to provide full coverage of the 10 divertor units. Three distinct imaging systems are utilized: Nine immersion tube systems [15] use microbolometer cameras with a detection wavelength range of 8–11 μm. Two advanced endoscope systems, integrated in plasma vessel module M3, are equipped with Stirling-cooled InSb cameras and a narrow-band filter that restricts detection to a wavelength of 4.85 μm. Two direct-view systems monitor the corner region of the vertical target and the baffle [16].

The effect of surface layers that are dynamically built by erosion, migration, and deposition processes during plasma operations has been considered in the analysis of surface temperatures. These layers, which consist of carbon, hydrogen, oxygen, boron, and metal impurities, have a higher surface temperature than the bulk material due to limited heat contact with the heat sink of the different components. In practice, the surface layer detection algorithm uses the results of a finite element method (FEM) simulation to estimate the temperature difference (ΔT_{FEM}) for each

TABLE 1 | W7-X magnetic field configurations used in OP2.2/OP2.3.

Configuration ID	I_1 (A)	I_2 (A)	I_3 (A)	I_4 (A)	I_5 (A)	I_A (A)	I_B (A)	iota(0)	Mirror ratio at $r = 0$	B_0 (T)	Number of discharges in OP2.2/OP2.3
EIM000+2520[a]	12,985	12,985	12,985	12,985	12,985	0	0	0.8563	0.0434	2.52	748
EIM000+2614[a]	13,470	13,470	13,470	13,470	13,470	0	0	0.8563	0.0434	2.614	83
EIM000−2620[a]	−13,500	−13,500	−13,500	−13,500	−13,500	0	0	0.8563	0.0434	−2.62	106
IKJ000+2520	13,527	13,145	12,518	11,900	11,518	−2705	2705	0.8764	0.0773	2.52	46
KJM008+2520[b]	13,231	12,858	12,244	11,639	11,266	0	0	0.8702	0.1002	2.52	262
KJM008+2620[b]	13,756	13,368	12,730	12,101	11,713	0	0	0.8702	0.1002	2.62	28
KJM008−2620[b]	−13,756	−13,368	−12,730	−12,101	−11,713	0	0	0.8702	0.1002	−2.62	87
AIM000+2520	12,732	13,276	13,276	14,365	14,365	0	0	0.84766	−0.0001	2.52	54
FTM000+2520[c]	14,187	14,187	14,187	14,187	14,187	−9783	−9783	1.0129	0.0544	2.52	135
FTM000+2620[c]	14,750	14,750	14,750	14,750	14,750	−10,171	−10,171	1.0129	0.0544	2.62	51
FTM000−2620[c]	−14,750	−14,750	−14,750	−14,750	−14,750	10,171	10,171	1.0129	0.0544	2.62	38
FMM002+2520	13,423	13,423	13,423	13,423	13,423	−3540	−3540	0.9095	0.0472	2.52	56
DBM000+2520[d]	11,863	11,863	11,863	11,863	11,863	8895	8895	0.7392	0.0348	2.52	82
KTM000+2520	14,888	12,819	12,819	12,819	12,819	−8844	−8844	1.0169	0.1024	2.52	4
DKJ000+2520	13,419	13,419	13,164	12,949	12,949	−3663	3100	0.873	0.0304	2.52	44
XIM001+2485	12,411	13,329	13,106	14,769	14,868	0	0	0.8444	−0.0199	2.485	55

[a]Standard configuration.
[b]High-mirror configuration.
[c]High-iota configuration.
[d]Low-iota configuration.
Source: W7-X magnetic field configurations database and W7-X logbook.

pixel. To compute this difference, the experimentally observed loading area must first be determined. This is achieved by grouping pixels according to the areas affected by the heat load. These areas, which may span more than one target element, are then segmented according to their respective elements. This is necessary since the elements are thermally isolated at the top surface due to slits and gaps. The discharge length is taken as the heating duration. It is important to note that thermal equilibrium with the cooling water is typically achieved within approximately 3 s for the target modules with carbon-fiber composite (CFC) materials. Under these conditions, the measured surface temperature can be related to a specific heat flux density, and vice versa. By contrast, equilibrium is usually reached within about 3 min in the central, horizontal divertor area (target modules TM5h and TM6h).

The temperature decay (ΔT_{exp}) following termination of heating power (NBI + ECRH) is calculated for each pixel across the 12 IR cameras for every discharge. These values are then compared with the corresponding results obtained from a FEM database analysis (ΔT_{FEM}). The FEM model solves the thermal conduction equation for the heat sink design of the water-cooled divertor components—specifically, the high-flux divertor modules and the baffle-like structures of the middle divertor parts—to determine the surface temperature decay after the heating is turned off, assuming there are no deposited layers. The target element's geometry and material properties, along with the experimental water-cooling condition, are taken into account. The temperature drop for the experiment and the FEM database is taken within 0.1 s of power-off in each case. Based on these results, a database is created and used in the evaluation after each discharge. Pixels corresponding to a surface layer are identified and excluded from the maximum temperature evaluation when ΔT_{exp} exceeds $1.1 \times \Delta T_{FEM}$. The factor of 1.1 serves here as a conservative safety margin, which was determined based on an empirical assessment by the technical team to ensure operational safety. Both the FEM calculations and the surface layer detection algorithm consider three key factors influencing the temperature decay time:

1. *Loading area*: A smaller loading area—such as a single pixel—results in faster temperature decay, as heat diffuses laterally to adjacent pixels. For the FEM database, the loading area ranges from 3×3 mm^2 to 53×25 mm^2 (full CFC tile size of a target element).
2. *Initial temperature at power-off*: A higher initial temperature usually results in faster decay. For the FEM database, the surface temperatures are calculated with different loading areas when the input heat flux ranges from 1 to 10 MW/m^2 (increments of 1 MW/m^2).
3. *Duration of heating pulse*: Decay is faster when the heating duration is shorter, particularly when the component remains relatively cold overall. The duration of the heating pulse has a strong effect on the middle divertor part. Thus, different durations were applied in the FEM calculations to create a database: 2, 5, 10, 20, 30, 60, 120, and 1800 s.

Using the experimentally determined loading area, maximum temperature, and pulse length, multidimensional interpolation is performed with the database to obtain ΔT_{FEM}, which is then compared to ΔT_{exp}.

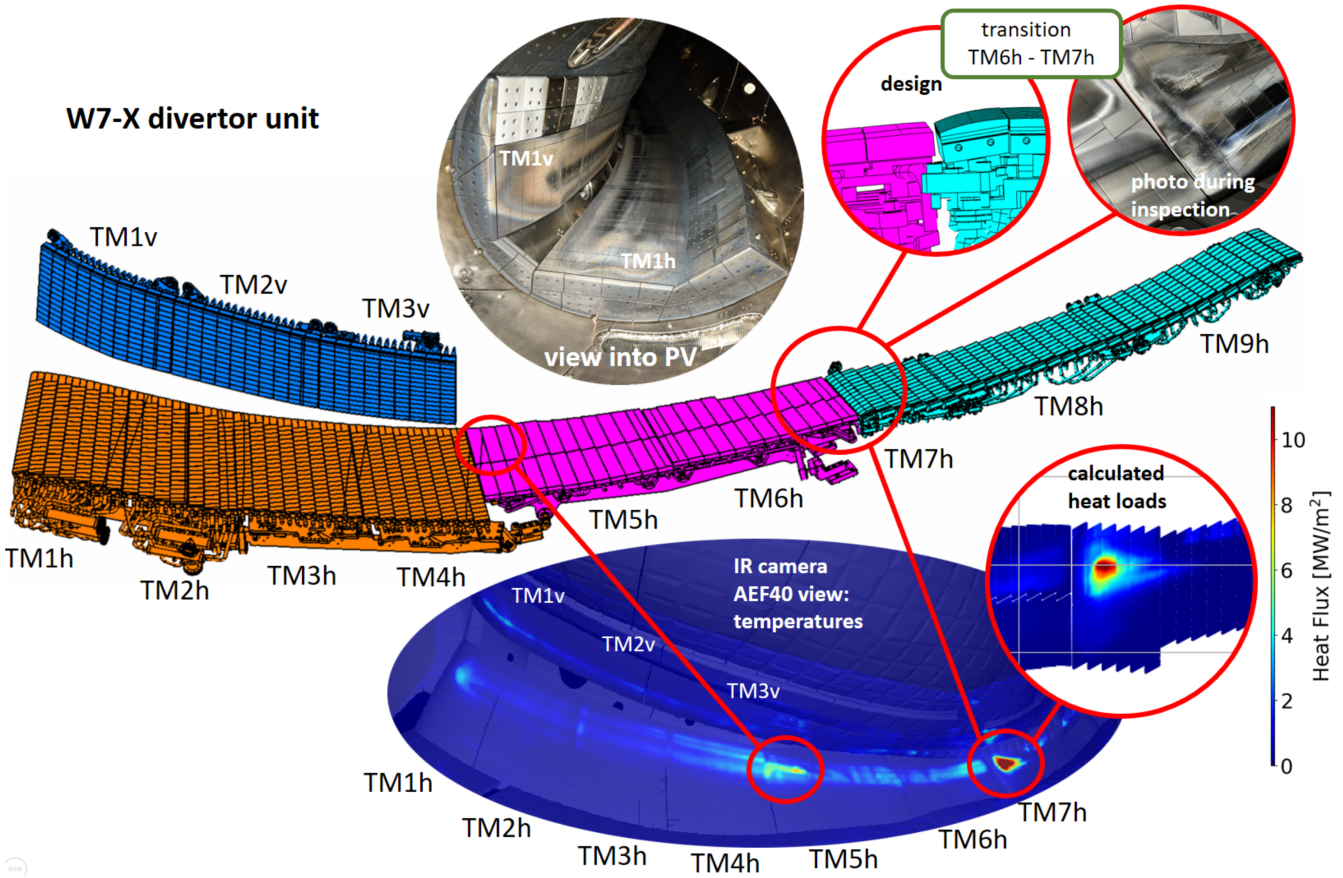

FIGURE 1 | One of the 10 water-cooled divertor units of the W7-X is shown, with the different target modules indicated. TM1h–TM4h belong to the low-iota divertor area (in orange); TM5h and TM6h are the middle part of the divertor and have a baffle-like design (in purple); and TM7h–TM9h represent the high-iota part of the divertor (in cyan). TM1v–TM3v are the three vertical target modules (in blue). Each CFC target module consists of separate target elements, or "fingers." A photo showing the view into the plasma vessel is given at the top. Due to the toroidal geometry, only the low-iota divertor area together with the vertical targets is visible. The critical excess heat load positions (TM5h and TM7h) are highlighted with design details and a photo taken during an inspection of the lower divertor unit of plasma vessel module M4. Temperature measurements taken by the AEF40 camera monitoring this divertor unit are also shown as an example, as well as the calculated heat loads (discharge XP_20250408.051 at 2.2 s with EIM000+2520).

Calculating heat loads based on measured surface temperatures requires significant development of the applied 3D finite-difference model to account for the effect of thermally weakly bonded layers through special boundary conditions. This work is underway, and results for all discharges of the OP2.2 and OP2.3 campaigns are expected by May 2026.

2.2 | Heat Load Criticality

The maximum surface temperatures of the various target modules have now been arithmetically averaged based on the discharges of a specific magnetic field configuration as given in Table 1. Regardless of which IR camera detected them, the maximum temperature values were taken into account for a specific target module. The criticality κ is obtained by dividing these averaged maximum temperatures by the technical temperature limit specified for the target modules, $\kappa = T_{\text{max, av}}/T_{\text{limit, module}}$. A criticality value above unity, therefore, indicates that the target module is operating beyond its specified heat-load capability. The W7-X divertor unit consists of nine horizontal target modules (TM1h–TM9h), as shown in Figure 1. The target modules TM5h and TM6h, which are in the middle, have limited cooling. Their temperature limit is 650°C. The other horizontal target modules, as well as the three vertical target modules (TM1v–TM3v), have a maximum allowed surface temperature of 1200°C. The results obtained for the 16 selected configurations, including the reversed field configurations EIM000−2620 and FTM000−2620, are given in Figure 2. All configurations used in the last two campaigns were reviewed. However, only a representative sample of the configurations was selected based on operation time and criticality. Notably, many of the discharges in the high-iota configurations (FTM000+2620 and FTM000−2620) resulted in temperatures for the TM6h and TM7h modules that were very close to or above the critical limit. This is significant because these criticality values are obtained by averaging a set of discharges. This presentation clearly shows enhanced heat loads on the vertical targets, especially on TM1v, in the high-mirror configurations. However, these loads have not posed a critical operational issue.

A general trend observed for nearly all configurations is the critical temperatures of the horizontal target modules: TM5h, TM6h, and TM7h. These results quantify the observation made during the campaign that the limitations of these modules restricted

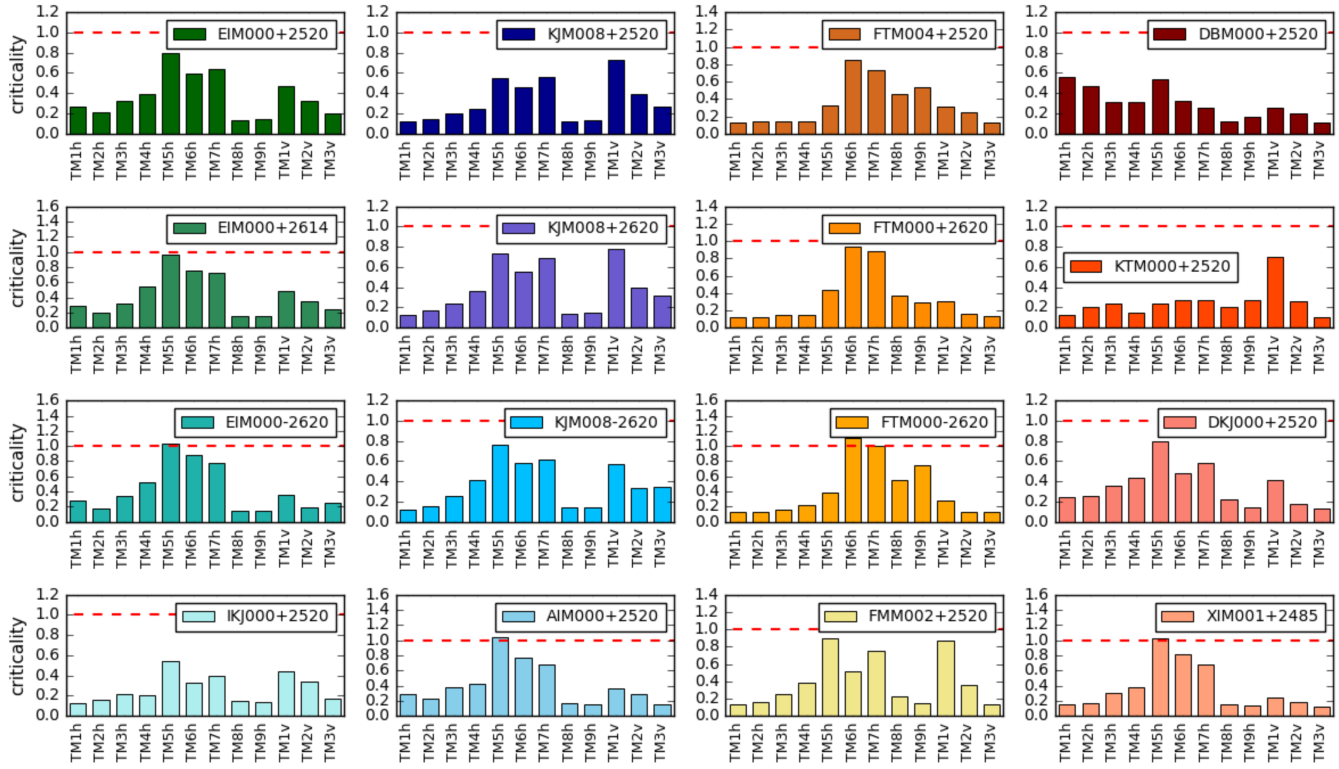

FIGURE 2 | This is a comparison of the heat load footprints on the divertor targets of different magnetic field configurations that were run in W7-X during campaigns OP2.2 and OP2.3. The relevant configuration is indicated in the legend of each figure. Results are shown for the horizontal (TM1h–TM9h) and vertical (TM1v–TM3v) target modules. The criticality limit, $\kappa = 1$, is indicated by a red dashed line. See Section 2.2 for the definition of κ.

plasma operation, particularly with regard to further increases in heating power. The high surface temperatures observed on TM6h are likely the result of a combination of factors. First, there is a finite scene-model mismatch in the IR system (the IR emission from the TM7h spot could be incorrectly assigned to the neighboring TM6h position), which is difficult to improve; otherwise, the mapping in other areas (TM1h–TM4h and TM1v–TM3v) would be compromised. Second, there is a potential optical effect, which involves blurring of the intense hot spot in the initial target element of the TM7h target module. Furthermore, in instances where critical situations were detected at TM6h, the hot spot at TM7h exhibited temperatures that exceeded the 1200°C threshold. Both critical positions are shown in Figure 1. Only part of the module is affected, not the entire module. The load on the TM5h target module is due to an extension of the main strike line formed on the TM2h–TM4h modules for the standard and high-mirror configurations. At TM7h, increasing the magnetic field-line incidence angle to 7°–8° results in larger heat loads. At other divertor target locations, angles in the range of 0°–3° prevail. Figure 1 includes a zoomed-out picture of the design for the position at the transition between TM6h and TM7h. This illustrates the curvature of the first element of TM7h, which results in larger incidence angles. This curved design of the first target element of TM7h was necessary to compensate for the lowering of TM6h, which was initially aiming to reduce the heat load on the middle part of the divertor (TM5h, TM6h). However, this attempt was unsuccessful due to higher-than-predicted plasma transport into the target-shadowed regions (TSRs). This also caused larger heat loads at the beginning of TM5h, as mentioned above. These regions are characterized by rather short connection lengths below 35 m because they are shadowed ("protected") by other divertor units in the torus. Unlike private flux regions (PFRs), which have connection lengths of about 100 m, TSRs are not in contact with confined regions [17].

For the standard configuration EIM000+2520, which was used for most discharges in OP2.2/2.3 (Table 1), the criticality values are shown in Figure 3 as a function of the line-integrated electron density (n_e) and the scrape-off-layer power P_{SOL} for selected target modules (as indicated in the legends of the subplots). For P_{SOL}, the heating power of both the ECRH and NBI systems is added, and the radiated power measured by bolometry [18] is subtracted, $P_{SOL} = P_{ECRH} + P_{NBI} - P_{rad}$. These values are taken at the moment of maximum surface temperature during a discharge. As expected, higher convective power results in higher loads and subsequently higher surface temperatures, as seen for the TM4h module loaded by the main strike line in this configuration (upper left subplot in Figure 3). The TM9h target module remains largely unaffected. This module is loaded in high-iota configurations, but not in standard configurations.

The TM5h target is loaded to the limit in almost all plasma discharges. There is no notable dependence on plasma density for the TM4h module, but there is for the TM7h module: higher plasma density results in higher surface temperatures. This supports the findings that there are different transport characteristics for the main scrape-off layer (SOL) plasma and the TSRs [19].

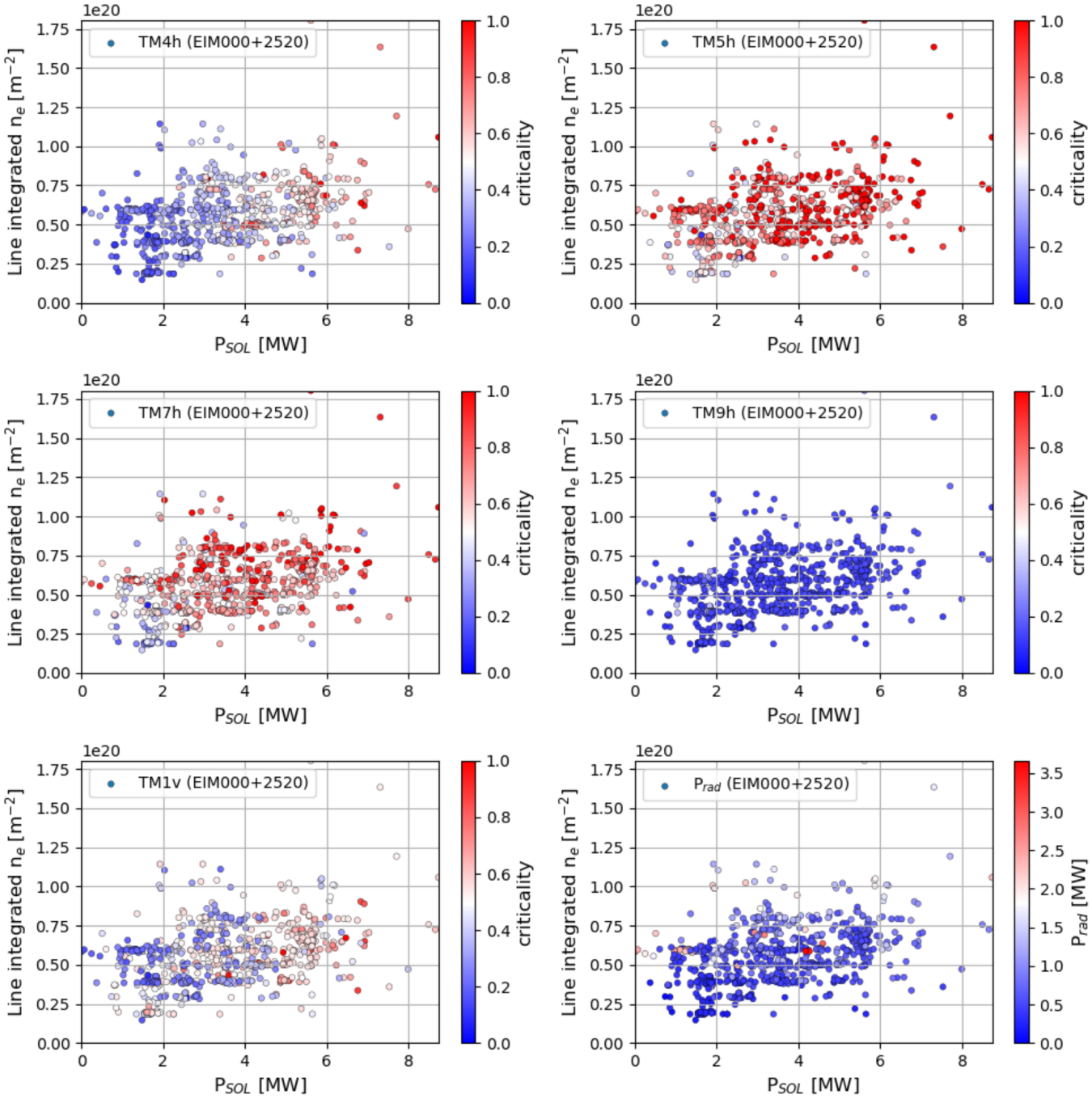

FIGURE 3 | Criticality as a function of line-integrated electron density (n_e) and P_{SOL}, the difference between the external heating power ($P_{ECRH} + P_{NBI}$) and the radiation losses (P_{rad}). In these scatter plots, criticality is color-coded, with critical values close to unity shown in red. Each symbol represents the plasma/heating parameters and surface temperature criticality for one discharge in the standard magnetic field configuration EIM000+2520, with a total of 748 discharges from the OP2.2 and OP2.3 campaigns represented. As shown in the legend, the results correspond to the different target modules: TM4h, TM5h, TM7h, TM9h, and TM1v. In the bottom-right subplot, the radiation losses are color-coded for the same set of discharges.

The corresponding radiation power values are shown in the bottom-right subplot as a function of P_{SOL}. Relatively low values of radiated power dominate because these values correspond to the moment in time during the discharge when the maximum temperature is detected. It is worth noting that this analysis does not include certain parameters, such as the current settings of the control and trim coils or the toroidal plasma current, to focus on the main trends and to demonstrate the weak design points of the current geometry setup.

The current middle divertor targets (TM5h and TM6h) are baffle-like structures with graphite tiles for top cladding. They have a heat load capability of less than 1 MW/m^2 and a maximum allowed surface temperature of 650°C. In nearly all W7-X

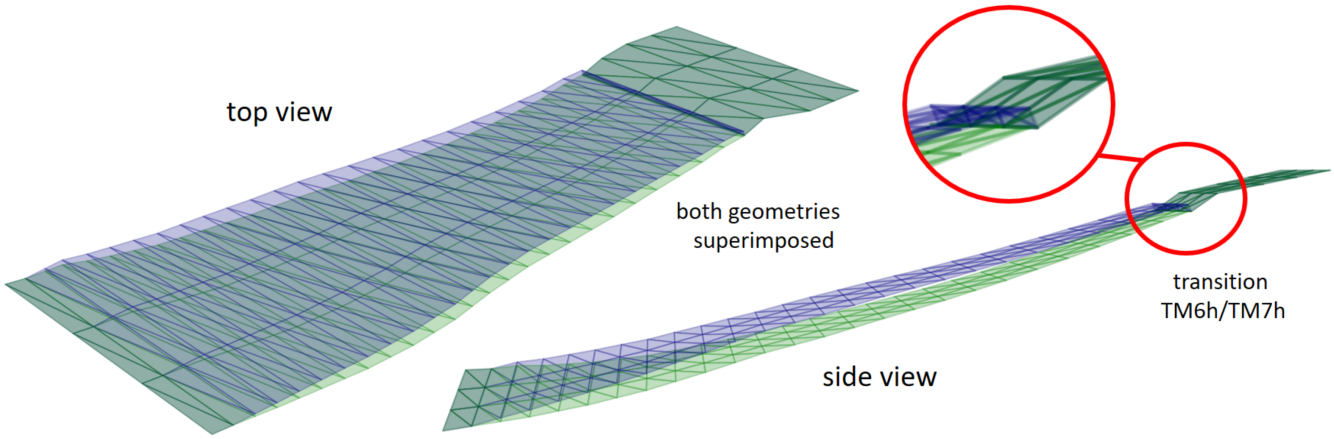

FIGURE 4 | The numerical grids are shown in green for the current setup and in blue for the modified geometry of the middle part of the divertor. The transition at TM6/TM7h is shown enlarged.

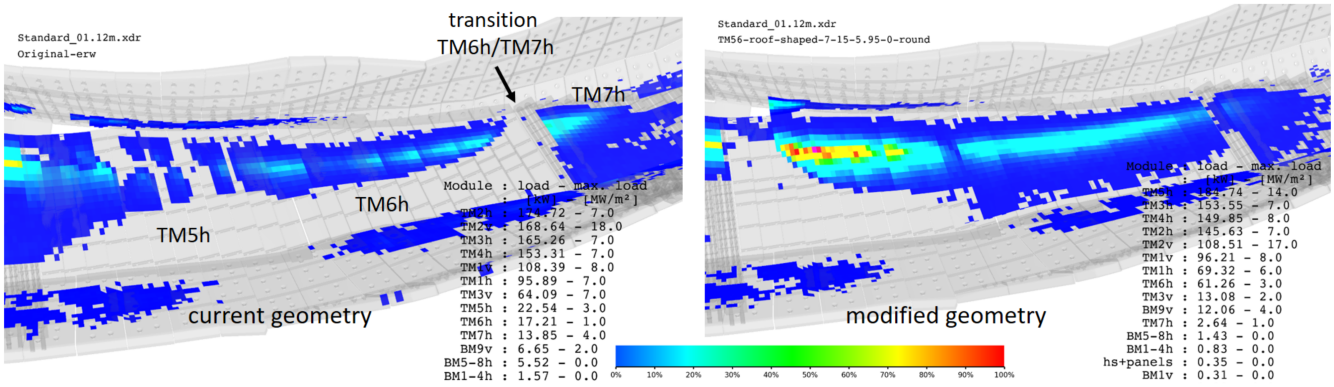

FIGURE 5 | Results of EMC3-Lite heat-load calculations for the standard magnetic field configuration (with $\beta = 2\%$, $I_{tor} = 0\,kA$) shown for the current setup (left figure) and for the modified middle-divertor geometry (right figure). The TM5h, TM6h, and TM7h divertor modules are shown alongside adjacent baffle modules. The color bar is displayed with 100% representing 10 MW/m^2. These presentations include detailed information about the power input in kW for each component, as well as the peak heat flux density in MW/m^2.

magnetic field configurations, unexpectedly high transport into the TSRs leads to loads and surface temperatures that exceed the specified limits.

3 | Middle Divertor Modification

Based on the results obtained in Section 2, modifying the target geometry of the middle divertor could help overcome operational restrictions and limitations of heating energy. The idea is to replace these modules with ones that can withstand much higher loads, ideally up to 10 MW/m^2. Furthermore, a roof-shaped design of this divertor part reduces the loads on the adjacent high-heat-flux (HHF) module TM7h without modifying its position.

The height of the "roof" was optimized to balance the maximum permitted heat loads on TM5h/6h with the desired load reduction for TM7h. Heat load calculations for the original and the modified geometries have been performed by using the recently developed EMC3-Lite code [20]. EMC3-Lite takes into account two types of conduction: parallel classical electron conduction and perpendicular anomalous conduction. Both processes prevail at low plasma densities. In our EMC3 modeling, the following input parameters are used for the plasma edge: an averaged plasma density of 10^{19} m^{-3}, an electron temperature of 100 eV, and an energy diffusion coefficient of 2 m^2/s. Several parameter sets were examined based on experimental results. This set was chosen because it is conservative. The various transport processes of particles are not considered in this code (neither for the fuel nor impurity ions); however, the Bohm boundary condition is applied, requiring the particles to flow toward a surface and reach the isothermal sound speed at the sheath entrance. It is noteworthy that the code is three orders of magnitude faster than traditional field-line tracing. This is due to the implementation of the reversible field-line mapping (RFLM) technique [21]. This method involves the reconstruction of continuous field lines from field lines of finite length that have been pre-calculated.

In the present study, a heating power of 10 MW was employed in all EMC3-Lite calculations. The corresponding numerical grids showing the plasma-facing surface are displayed in Figure 4. The results are shown in Figure 5 for the standard magnetic field configuration and in Figure 6 for the high-iota configurations and selected β and I_{tor} values. These two configurations are considered in the design optimizations with variations in

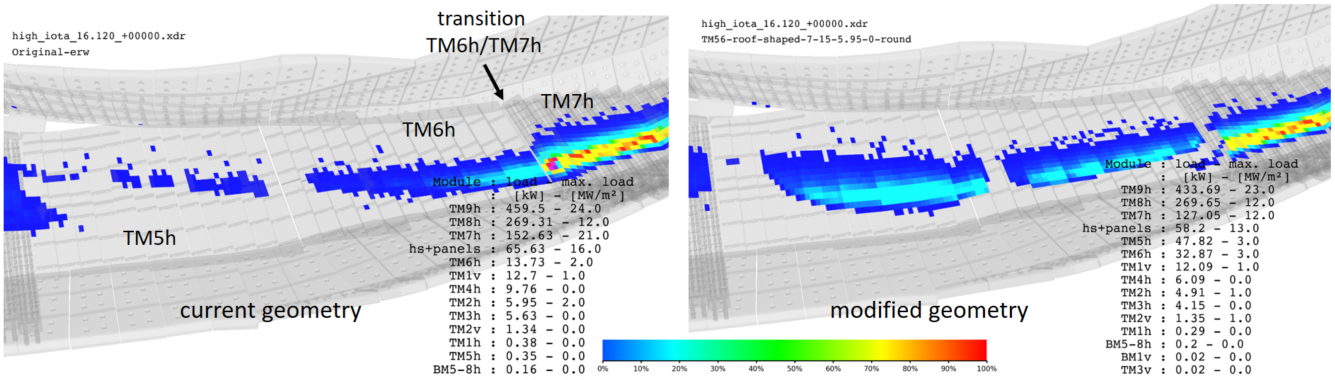

FIGURE 6 | Results of EMC3-Lite heat-load calculations for the high-iota magnetic field configuration (with $\beta = 2.4\%$, $I_{tor} = 0$ kA) shown for the current setup (left figure) and for the modified middle-divertor geometry (right figure). The TM5h, TM6h, and TM7h divertor modules are shown alongside adjacent baffle modules. The color bar is displayed with 100% representing 10 MW/m^2.

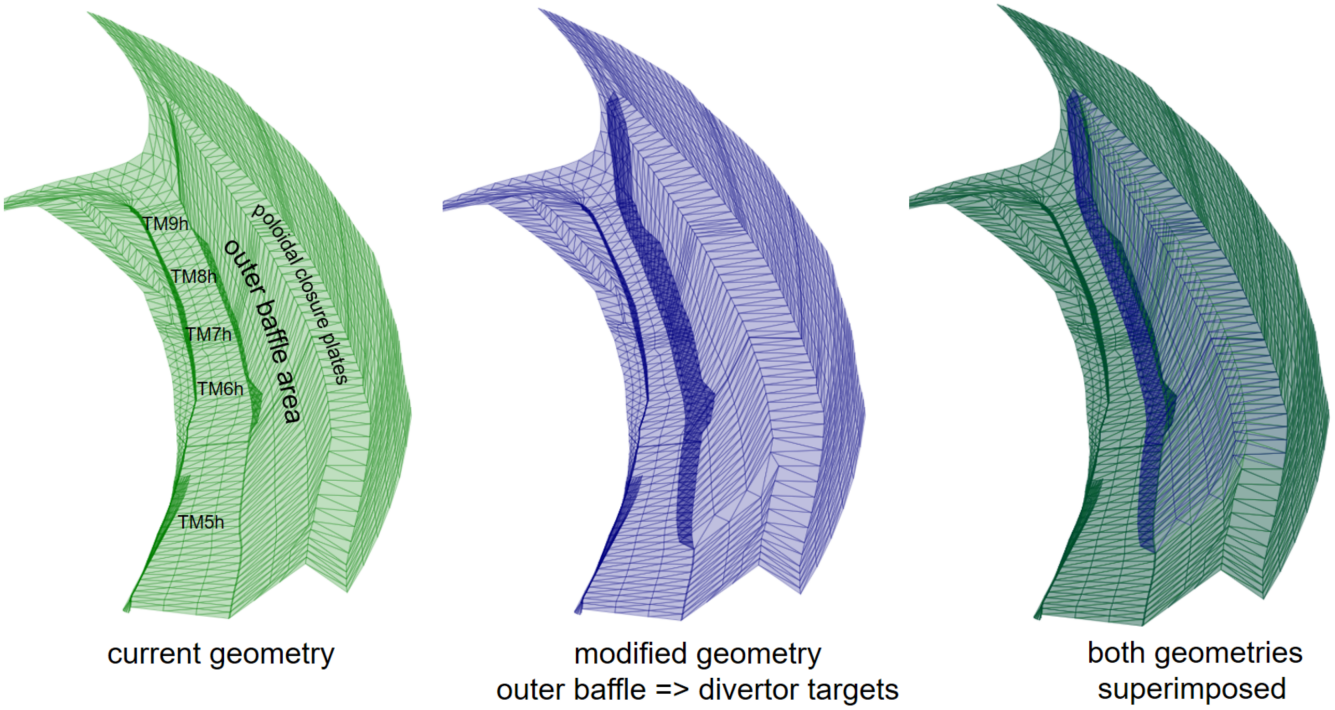

FIGURE 7 | These are the numerical grids used for the EMC3-Lite calculations. The grid on the left represents the current geometry setup of the plasma-facing surfaces built by the divertor targets, baffle areas, and first wall components. Center: A modified numerical grid in which the outer baffle was moved toward the plasma to redistribute the heat loads on these surfaces. Right: Both geometries are shown to illustrate the modifications. The modified area of the former outer baffle is labeled "ODT" (outer divertor target) in the following.

plasma pressure and volume-averaged beta values up to 2.5% and toroidal currents I_{tor} in the range of −20 to +20 kA. The magnetic fields necessary for the heat load calculations with EMC3-Lite were provided by VMEC-EXTENDER simulations [22]. These simulations are capable of generating the magnetic field in MHD equilibrium for the confined region with nested magnetic flux surfaces, as well as the fields outside the LCFS in the edge plasma with the characteristic island chains, where a certain level of stochasticity can also be considered. To this end, the VMEC solution is integrated with the EXTENDER fields (obtained by employing the virtual casing principle) and the fields by the external coils (via Bio-Savart).

Due to the geometry change, the thermal load onto the first target element of TM7h is significantly reduced in the high-iota configuration (Figure 6). This element is situated within the shadow of the roof-shaped structure of TM5h/6h, as the plasma is flowing toward this position of the first target element from the low-iota part of the divertor, that is, from TM1h to TM4h. For the subsequent target elements (or target fingers) of TM7h, the plasma is flowing from the opposite direction, that is, from TM9h to TM8h. The "watershed" in the incidence angle distribution is located poloidally between the first and second target elements of TM7h. This is also the case for the standard configuration. Nevertheless, a decrease in the heat loads is evident for the standard

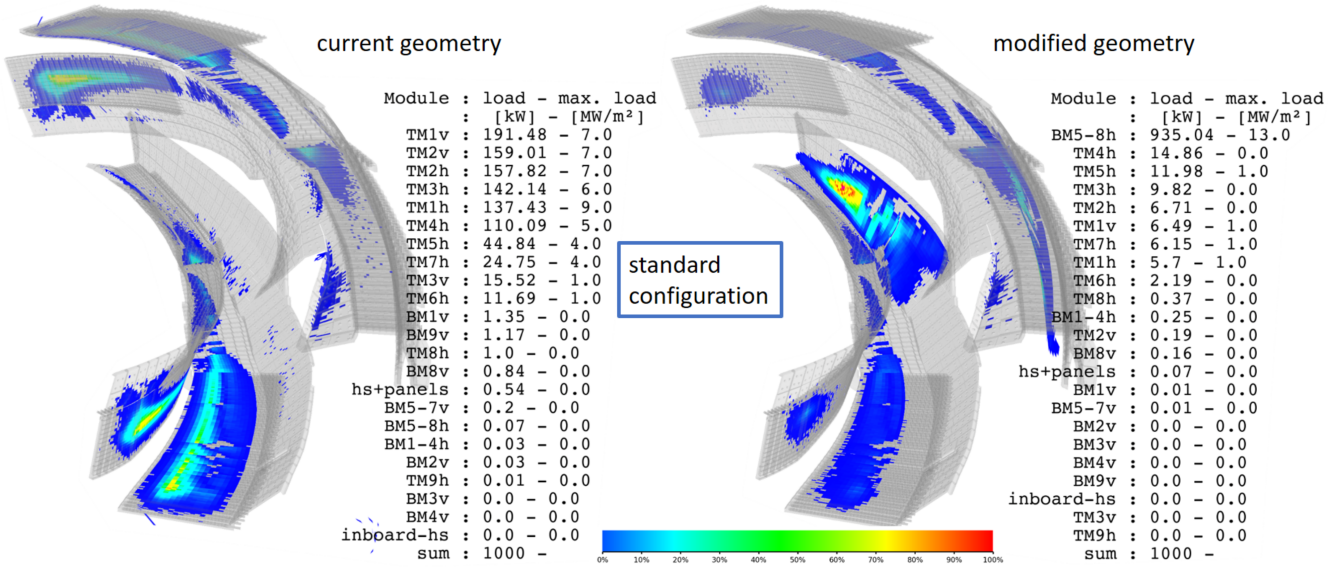

FIGURE 8 | Results of EMC3-Lite heat-load calculations for the standard magnetic field configuration (with $\beta = 1.32\%$, $I_{tor} = +12$ kA) shown for the current setup (left figure) and for the modified outer baffle geometry (right figure). This image shows a W7-X plasma vessel module. The divertor units are at the top and bottom. Looking down, one can see the TM1h–TM9h target modules of the lower divertor unit, as well as the outer baffle modules. The color bar is displayed with 100% representing 10 MW/m^2. The loads on the inward-moved ODT are given under the notation BM5-8h on the right figure.

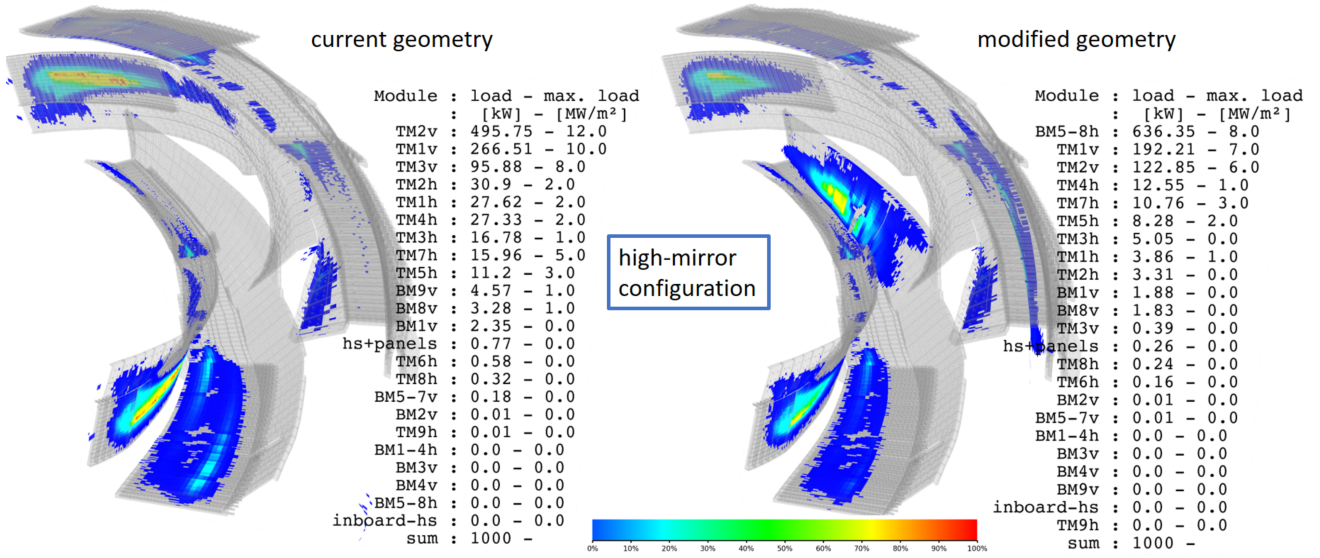

FIGURE 9 | Results of EMC3-Lite heat-load calculations for the high-mirror magnetic field configuration (with $\beta = 2\%$, $I_{tor} = +10$ kA).

configuration, not only for the first target element but also for the remaining part of TM7h (Figure 5). This can be discussed in the framework of the developed concept of "power-carrying layers" [19, 23]. These layers are associated with long connection lengths of several hundred meters. The loads of neighboring surface elements can be described as a function of distance to these layers, according to a simple exponential ansatz. The modified middle divertor results in the scraping of the power-carrying layers for the standard magnetic field configuration. For the hot spot on TM7h, the loads are reduced due to the slight increase in distance from these power channels. In the high-iota configuration, the power-carrying layers are situated at a higher position within the middle divertor. These layers are less influenced by the roof-shaped structure of the newly proposed design. In this configuration, the protective effect is largely limited to the first target element of TM7h. Subsequent analyses will entail the optimization of the design by taking additional magnetic field configurations into account.

4 | Outer Baffle Modification

There is an alternative option for reducing thermal loads in the middle part of the divertor (TM5h/TM6h) and protecting the TM7h target module without modifying the installed water-cooled divertor modules at all. The outer baffle modules

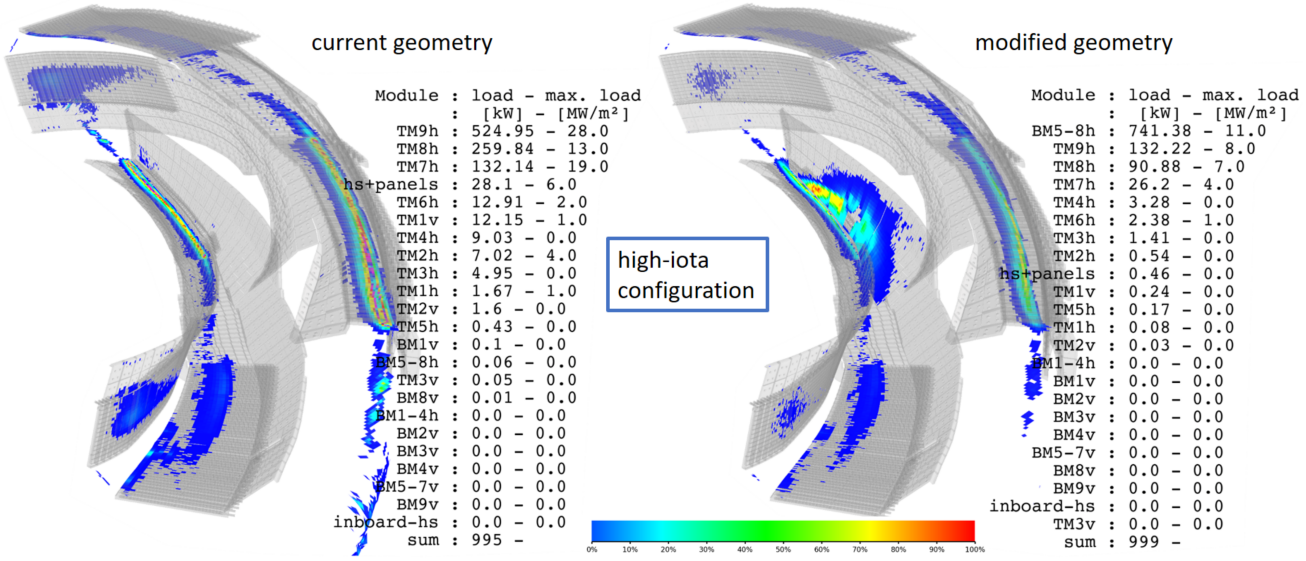

FIGURE 10 | Results of EMC3-Lite heat-load calculations for the high-iota magnetic field configuration (with $\beta = 1.2\%$, $I_{\mathrm{tor}} = +10\,\mathrm{kA}$).

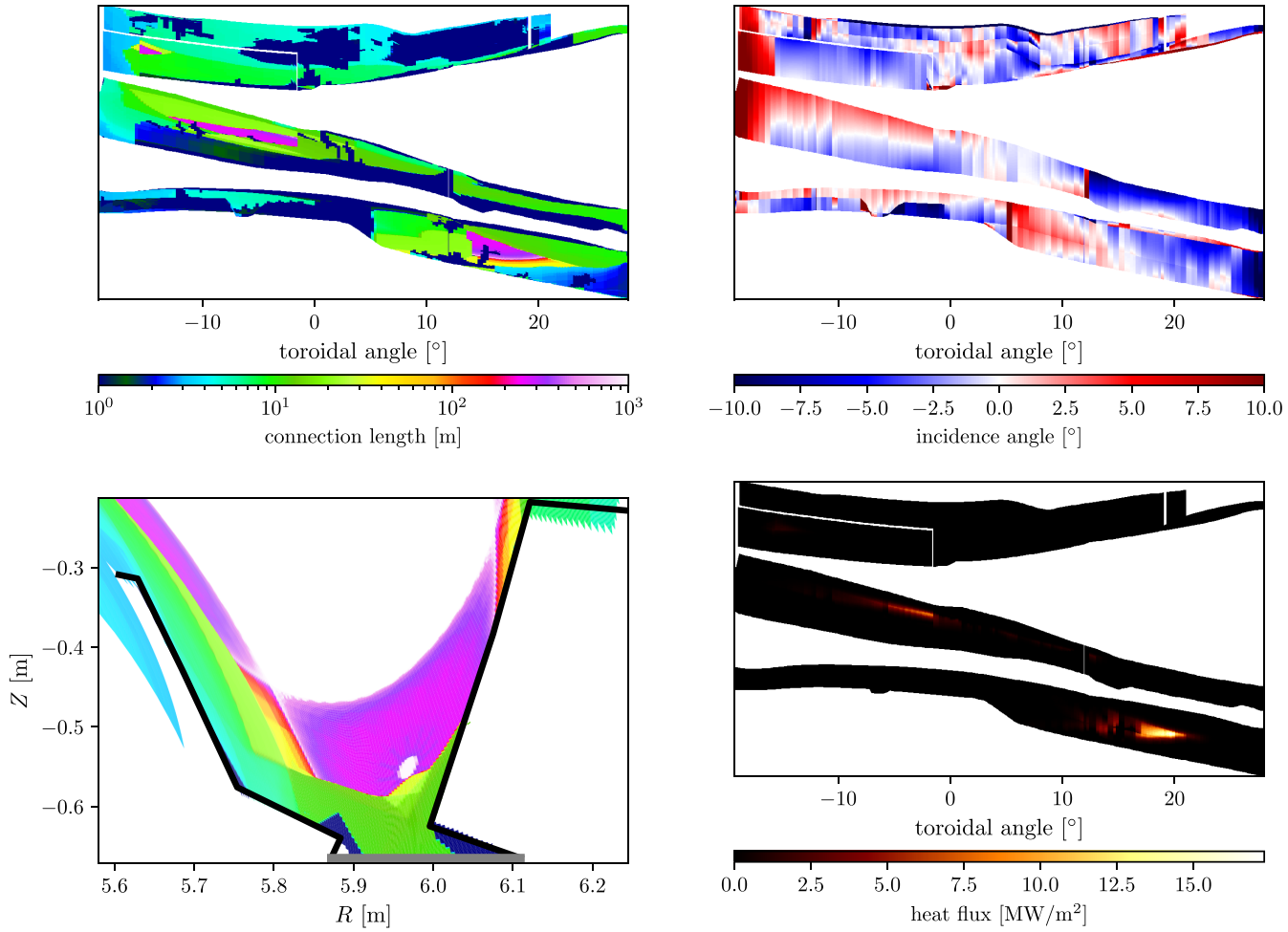

FIGURE 11 | Connection lengths distribution (top left subplot), incidence angles (top right), and heat flux densities (bottom right), mapped onto a 2D presentation of the divertor and baffle modules of one W7-X divertor unit for the standard magnetic field configuration. In addition, the connection lengths are displayed on a poloidal cross-section at $\phi = 18^{\circ}$. The private flux regions (PFRs) are shown in red colors in the left subplots near the x-points, and the target shadow regions (TSRs) are shown in green cyan.

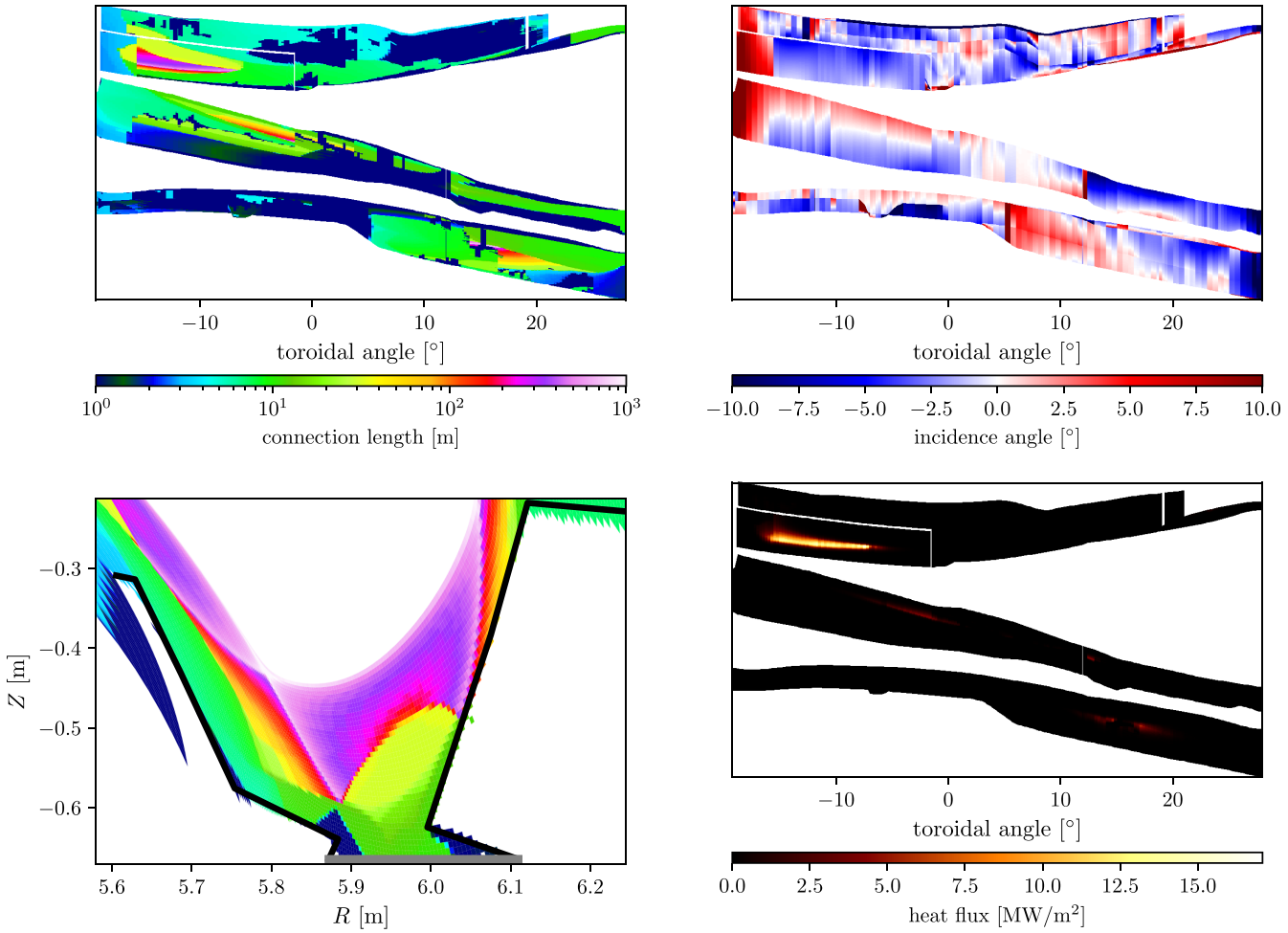

FIGURE 12 | As in Figure 11 for the high-mirror magnetic field configuration.

could be replaced by divertor targets, which are positioned further inward than the current outer baffle surfaces, as seen in Figure 7. These new targets should be able to handle loads of up to 10 MW/m^2 instead of the maximum of 500 kW/m^2 that is specified for baffle modules. A variety of geometries have been examined for three magnetic field configurations, considering different β values and various toroidal plasma currents (I_{tor}). The heat loads calculated with EMC3-Lite are shown for the standard configuration (Figure 8), the high-mirror configuration (Figure 9), and the high-iota configuration (Figure 10) for the parameters as given in the respective figure captions. These results were obtained using the design of the ODT that performed best. Once more, a heating power of 10 MW was utilized in the EMC3-Lite calculations.

The subplots on the left side show the well-known characteristic heat load pattern of the different configurations for the current setup. The main strike lines are visible for the standard configuration on the horizontal targets TM1h–TM4h and on the vertical target modules TM1v–TM3v (Figure 8). In the high-mirror configurations (Figure 9) with the main strike line on the vertical targets, strike lines on the horizontal target modules are less pronounced. As the results presented here are calculated with a higher β value, a second strike line appears on the horizontal target, closer to the outer side of the plasma vessel. This is due to the modified island topology at higher plasma pressures [24]. The high-iota configuration justifies the name of the high-iota section of the divertor (TM7h–TM8h) since it is the main interaction zone (Figure 10). The rather sharp strike lines with high peak loads have a comparable high resilience, for example, against changes in control coil currents.

On the right side of these three figures, the results are presented for the modified geometry. It is noteworthy that the loads are redistributed from the other target modules toward the new divertor target (ODT) for all three different magnetic field configurations. In principle, it is feasible to reduce the loads on the other target modules even further, down to baffle limits, by adjusting the ODT slightly more inwardly than was selected for the calculations presented here. However, this approach is accompanied by a trade-off involving significant divertor functions. The target would be in close proximity to the confined region, which would pose a risk of it acting as a limiter. This is especially true for the high-iota configuration. To illustrate this, the distributions of connection lengths, incidence angle of the magnetic field lines, and the heat loads calculated with EMC3-Lite (here for the vacuum magnetic fields) are given in Figure 11 for the standard configuration and in Figure 12 for the high-mirror configuration. Figure 13 shows the results for a modified high-iota configuration with a high mirror ratio ($I_1 = 15{,}316$ A, $I_2 = 12{,}605$ A, $I_3 = 12{,}605$ A,

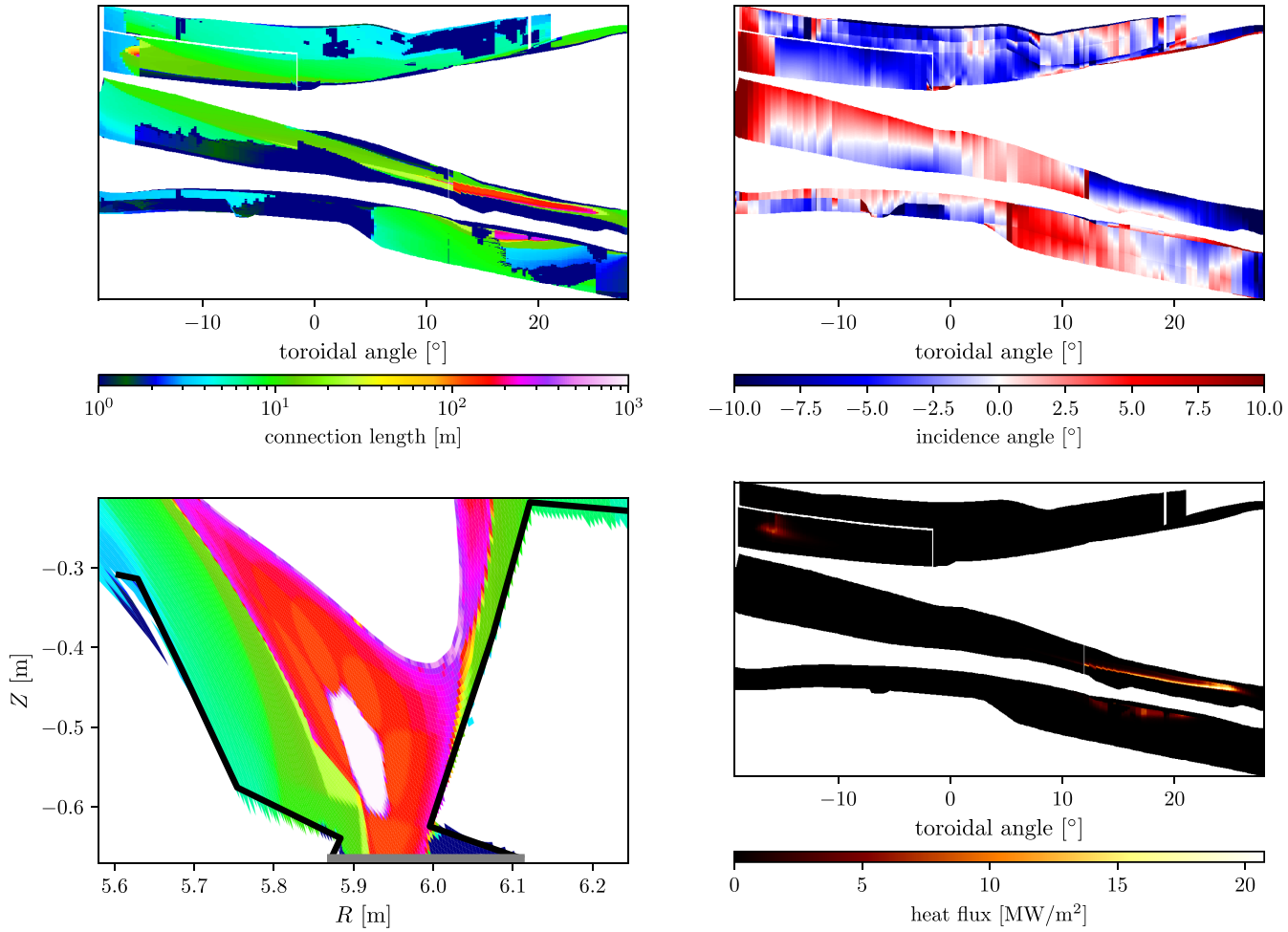

FIGURE 13 | As in Figure 11 for a modified high-iota magnetic field configuration ($I_1 = 15{,}316$ A, $I_2 = 12{,}605$ A, $I_3 = 12{,}605$ A, $I_4 = 12{,}605$ A, $I_5 = 12{,}605$ A, $I_A = -10{,}262$ A, $I_B = -10{,}262$ A).

$I_4 = 12{,}605$ A, $I_5 = 12{,}605$ A, $I_A = -10{,}262$ A, $I_B = -10{,}262$ A) to move the confined region away from the outer target. The two plots in the top row and the right plot on the bottom use a special 2D presentation. It is not a correct 2D mapping of a view from above; rather, the loads are shown on unfolded surfaces of the divertor and baffle components of one of the 10 divertor units (load symmetry is assumed in the EMC3-Lite calculations). The inboard baffle modules are shown above the divertor targets, and the outboard baffles are shown below them. Note that the y-axis is not representative of the actual dimensions of the components in space. However, the x-axis coordinates (toroidal angles) indicate the toroidal position of each module. The bottom left plot displays the distribution of connection lengths on a poloidal cross-section at the toroidal position of $\phi = 18^\circ$. This cross-section is located in the center of the ODT, which has been moved inward toward the plasma. For these calculations, the same modified geometry as in Figure 7 is used.

5 | Summary and Outlook

As shown in Section 2.2, plasma operation in OP2.2/2.3 resulted in surface temperatures of target modules approaching their technical limits under attached plasma conditions. In particular, the horizontal target modules TM5h and TM7h were affected for most of the magnetic field configurations used in the W7-X stellarator during these operation campaigns, despite considerable efforts to mitigate the loads by using the control and trim coils, as well as adjusting the plasma toroidal current via ECCD. Only heavy impurity seeding considerably reduced the convective loads, resulting in a high level of radiation in the edge plasma and leading to detached conditions. Due to active seeding with impurities, the resulting radiation zones could move within the confined region, which would deteriorate the plasma profile gradient required for optimal core performance. This is a concern for upcoming campaigns with the planned increase in heating power. This paper discusses two possible technical solutions to mitigate excess heat loads in specific locations on single target modules. Both require replacing the current modules with heat sink components newly developed in the EUROfusion framework (work package WPDIV) [25]. These components must be able to withstand heat loads significantly higher than the 1 MW/m^2 limit of the current middle part of the divertor.

The first option is a roof-shaped design for the TM5h and TM6h target modules (Section 3). This design also protects the adjacent TM7h target module, where hot spots on the first target elements are mitigated by the shadow of the modified TM5h/TM6h surface

structure. The height of the roof's protrusion toward the plasma largely depends on the final heat load capability of the replaced targets.

The second option involves replacing outer baffle modules with ODT. With the proposed modifications to the plasma-facing surface, heat loads can be redistributed from the other target modules to this new target surface (Section 4). This works for the main magnetic field configurations of the W7-X, such as the standard and high-mirror configurations. With some adjustments, it also works for the high-iota configurations. Notably, a much smaller surface area would suffice for these configurations, which currently require 2.5 m^2 for one divertor unit (see Figure 1). However, implementing this more radical design change would require a far greater technical effort than modifying the middle part of the divertor units (e.g., TM5h/6h). The current set of diagnostics (including IR thermography) would not suffice for observation here, and modifications and new developments would be necessary.

While these design changes meet the heat load constraints, other considerations are a cause for concern. For certain configurations, especially those with modified island topologies due to control and trim coil operation, toroidal plasma currents, and plasma pressure effects (higher β-operation), the confined region can be very close to the new target surfaces, within centimeters—which is especially critical for outward-shifted magnetic field configurations. Under certain plasma conditions, the penetration depth of the emitted molecule through the edge plasma could exceed this distance, resulting in dissociation and ionization processes inside the confined region. This is unfavorable for building the required plasma density above the divertor target for high recycling and efficient exhaust of the neutrals. The efficiency of exhausting neutrals is primarily determined by maintaining a sufficiently high level of neutral gas pressure in the sub-divertor space. This level has not yet been reached in W7-X experiments, which show neutral gas pressures below 0.1 Pa [26, 27]. The retention of impurities in the divertor, as well as the radiation capabilities of the resulting, rather thin, SOLs, could be affected, too. This is particularly important for magnetic field configurations such as high-iota configurations, since the radiation zone could end up in an unfavorable position (too close, or even within, the confined region), as discussed in [28]. These aspects of the outer divertor concept are planned to be studied using the 3D edge plasma transport EMC3-Eirene code [29, 30].

Specific modifications to the current geometry have been demonstrated to solve the observed heat load problems, providing valuable input to ongoing discussions on possible future hardware changes and allowing for a thorough evaluation of the pros and cons. These modifications would allow for an increase in heating power to achieve high core performance with significantly less effort than replacing all divertor targets. The long-term plan, however, is to develop divertor and baffle components with tungsten as the plasma-facing material [31] that can tolerate thermal loads, allow for high particle exhaust, and provide sufficient impurity control. These studies will use the developed tools that employ efficient, code-driven geometric transformations as input for the plasma codes. This allows for an accurate reflection of a stellarator's complex 3D topology at reduced resolution, enabling fast modeling. In particular, "closed" divertor geometries require restricting the flexibility of the magnetic field configuration space. Targets that serve to direct the recycling neutral particles away from the confined region [32] could lead to excessive local heat loads if the island topology is not perfectly aligned with the "closed" divertor targets.

Acknowledgments

This work has been carried out within the framework of the EUROfusion Consortium, funded by the European Union via the Euratom Research and Training Programme (Grant Agreement No 101052200—EUROfusion). Views and opinions expressed are, however, those of the author(s) only and do not necessarily reflect those of the European Union or the European Commission. Neither the European Union nor the European Commission can be held responsible for them. Open Access funding enabled and organized by Projekt DEAL.

Funding

This work was supported by the Euratom Research and Training Programme (101052200–EUROfusion).

Conflicts of Interest

The authors declare no conflicts of interest.

Data Availability Statement

Data available from the corresponding author upon reasonable request.

References

1. O. Grulke, C. Albert, J. A. Alcuson Belloso, et al., "Overview of the First Wendelstein 7-X Long Pulse Campaign With Fully Water-Cooled Plasma Facing Components," *Nuclear Fusion* 64 (2024): 112002.

2. T. Sunn Pedersen, M. Otte, S. Lazerson, et al., "Confirmation of the Topology of the Wendelstein 7-X Magnetic Field to Better Than 1:100,000," *Nature Communications* 7 (2016): 13493.

3. A. Dinklage, C. D. Beidler, P. Helander, et al., "Magnetic Configuration Effects on the Wendelstein 7-X Stellarator," *Nature Physics* 14 (2018): 855–860.

4. C. D. Beidler, H. M. Smith, A. Alonso, et al., "Demonstration of Reduced Neoclassical Energy Transport in Wendelstein 7-X," *Nature* 596 (2021): 221–226.

5. T. Sunn Pedersen, I. Abramovic, P. Agostinetti, et al., "Experimental Confirmation of Efficient Island Divertor Operation and Successful Neoclassical Transport Optimization in Wendelstein 7-X," *Nuclear Fusion* 62 (2022): 042022.

6. J. Boscary, A. Peacock, R. Stadler, et al., "Actively Water-Cooled Plasma Facing Components of the Wendelstein 7-X Stellarator," *Fusion Science and Technology* 64 (2013): 263–268.

7. S. A. Bozhenkov, O. Ford, M. Wappl, et al., "Routes to High-Performance Operation in Wendelstein 7-X (W7-X): Turbulence Suppression With Shaping of the Density Profile," paper presented at the 51st EPS Conference on Plasma Physics, Vilnius, Lithuania, July 7–11, 2025.

8. S. J. Meitner and L. R. Baylor, "Initial Commissioning Test Results of the Wendelstein 7-X Continuous Pellet Fueling System," *Fusion Science and Technology* 79 (2023): 1065–1070.

9. A. Dinklage, J. Baldzuhn, L. R. Baylor, et al., "Towards Steady-State Fusion: Demonstration of a Stable, Integrated High-Performance Scenario in the W7-X Stellarator," poster presented at the 51st EPS Conference on Plasma Physics, Vilnius, Lithuania, July 7–11, 2025.

10. S. A. Bozhenkov, M. Jakubowski, H. Niemann, et al., "Effect of Error Field Correction Coils on W7-X Limiter Load," *Nuclear Fusion* 57 (2017): 126030.

11. M. Endler, J. Baldzuhn, C. D. Beidler, et al., "Wendelstein 7-X on the Path to Long-Pulse High-Performance Operation," *Fusion Engineering and Design* 167 (2021): 112381.

12. Y. Gao, J. Geiger, M. Jakubowski, et al., "Effects of Toroidal Plasma Current on Divertor Power Depositions on Wendelstein 7-X," *Nuclear Fusion* 59 (2019): 106015.

13. J. Geiger, C. D. Beidler, Y. Feng, H. Maaßberg, N. B. Marushchenko, and Y. Turkin, "Physics in the Magnetic Configuration Space of W7-X," *Plasma Physics and Controlled Fusion* 57 (2015): 014004.

14. T. Andreeva, J. Geiger, A. Dinklage, et al., "Magnetic Configuration Scans During Divertor Operation of Wendelstein 7-X," *Nuclear Fusion* 62 (2022): 026032.

15. M. Jakubowski, P. Drewelow, J. Fellinger, et al., "Infrared Imaging Systems for Wall Protection in the W7-X Stellarator (Invited)," *Review of Scientific Instruments* 89 (2018): 10E116.

16. J. Fellinger, U. Lippmann, H. Greve, et al., "Design of Endoscopes for Monitoring Water-Cooled Divertor in W7-X," *Fusion Engineering and Design* 158 (2020): 111841.

17. Y. Gao, Y. Feng, M. Jakubowski, et al., "Understanding Baffle Overloads Observed in High-Mirror Configuration on Wendelstein 7-X," *Nuclear Fusion* 60 (2020): 096012.

18. D. Zhang, R. Burhenn, C. D. Beidler, et al., "Bolometer Tomography on Wendelstein 7-X for Study of Radiation Asymmetry," *Nuclear Fusion* 61 (2021): 116043.

19. A. Kharwandikar, "Power Exhaust Investigations in the W7-X Island Divertor," (PhD diss., University of Greifswald, 2025).

20. Y. Feng and W7-X Team, "Review of Magnetic Islands From the Divertor Perspective and a Simplified Heat Transport Model for the Island Divertor," *Plasma Physics and Controlled Fusion* 64 (2022): 125012.

21. Y. Feng, F. Sardei, and J. Kisslinger, "A Simple Highly Accurate Field-Line Mapping Technique for Three-Dimensional Monte Carlo Modeling of Plasma Edge Transport," *Physics of Plasmas* 12 (2005): 052505.

22. J. Geiger, C. D. Beidler, M. Drevlak, et al., "Effects of Net Currents on the Magnetic Configuration of W7-X," *Contributions to Plasma Physics* 50 (2010): 770–774.

23. D. Naujoks, A. Kharwandikar, V. Haak, et al., "Divertor Concept Development for the W7-X Stellarator Experiment," paper presented at the 4th Technical Meeting on Divertor Concepts, IAEA Headquarters, Vienna, Australia, November 7–10, 2022.

24. A. Knieps, Y. Suzuki, J. Geiger, et al., "Plasma Beta Effects on the Edge Magnetic Field Structure and Divertor Heat Loads in Wendelstein 7-X High-Performance Scenarios," *Nuclear Fusion* 62 (2022): 026011.

25. J. Fellinger, M. Richou, G. Ehrke, et al., "Tungsten Based Divertor Development for Wendelstein 7-X," *Nuclear Materials and Energy* 37 (2023): 101506.

26. V. Haak, S. A. Bozhenkov, Y. Feng, et al., "Overview Over the Neutral Gas Pressures in Wendelstein 7-X During Divertor Operation Under Boronized Wall Conditions," *Plasma Physics and Controlled Fusion* 65 (2023): 055024.

27. V. Haak, C. P. Dhard, D. Boeyaert, et al., "First Operation and Validation of Simulations for the Divertor Cryo-Vacuum Pump in Wendelstein 7-X," *Fusion Engineering and Design* 208 (2024): 114671.

28. Y. Feng, V. Winters, D. Zhang, et al., "Conditions and Benefits of X-Point Radiation for the Island Divertor," *Nuclear Fusion* 64 (2024): 086027.

29. Y. Feng, F. Sardei, J. Kisslinger, P. Grigull, K. McCormick, and D. Reiter, "3D Edge Modeling and Island Divertor Physics," *Contributions to Plasma Physics* 44 (2004): 57–69.

30. Y. Feng, H. Frerichs, M. Kobayashi, and D. Reiter, "Monte-Carlo Fluid Approaches to Detached Plasmas in Non-Axisymmetric Divertor Configurations," *Plasma Physics and Controlled Fusion* 59 (2017): 034006.

31. D. Naujoks, C. P. Dhard, Y. Feng, et al., "Performance of Tungsten Plasma Facing Components in the Stellarator Experiment W7-X: Recent Results From the First OP2 Campaign," *Nuclear Materials and Energy* 37 (2023): 101514.

32. F. Sardei, Y. Feng, J. Kisslinger, and W7-AS Team, "Island Divertors for Helical Devices," *Contributions to Plasma Physics* 40 (2000): 238–250.